

Dusty quasars eject star-forming gas from galaxies at cosmic noon

Hannah Stacey (✉ hrstacey@icloud.com)

Max Planck Institute for Astrophysics <https://orcid.org/0000-0002-8999-9636>

Tiago Costa

Max Planck Institute for Astrophysics

John McKean

University of Groningen

Eilat Glikman

Middlebury College

Paul van der Werf

Leiden Observatory, Leiden University

Physical Sciences - Article

Keywords:

Posted Date: February 22nd, 2022

DOI: <https://doi.org/10.21203/rs.3.rs-1355197/v1>

License:   This work is licensed under a Creative Commons Attribution 4.0 International License.

[Read Full License](#)

Dusty quasars eject star-forming gas from galaxies at cosmic noon

The canonical picture of galaxy evolution invokes the injection of energy from supermassive black holes to reduce star formation efficiency in massive galaxies^{1,2,3,4}. This process can explain^{5,6} their observed scaling relations, which were already established by cosmic noon (redshifts 2 to 3)⁷. However, the physical channels that allow energy and momentum released on sub-pc scales to affect gas on galactic scales are largely unconstrained^{8,9}. Here we report a direct link between quasar dust-reddening and molecular outflows at $z \sim 2.5$. By examining the dynamics of warm molecular gas in the inner region of galaxies, we detect outflows with velocities 700–1000 km s⁻¹ and short timescales of 0.05 Myr that are due to ongoing quasar energy output. We observe outflows only in systems where quasar radiation pressure on dust is sufficiently large to expel their obscuring gas column densities, indicating that radiative feedback regulates gas in the nuclear regions of galaxies. This is in agreement with theoretical models that predict radiation pressure on dust in the vicinity of the black hole is a major driving mechanism of galactic-scale outflows of cold gas^{10,11,12}. Our findings show that quasar radiation ejects star-forming gas from within nascent stellar bulges at velocities comparable to those seen on larger scales^{13,14} and that molecules survive in outflows even from the most luminous quasars.

Type 1 quasars are characterised by broad ionic emission lines (FWHM > 1000 km s⁻¹), with the majority having unobscured optical continuum emission, and 20–30 percent having reddened optical/infrared spectra¹⁵. The distinct properties of reddened quasars indicate that they are fundamentally different from their bluer counterparts^{16,17}, and it has been proposed that they represent a transitional stage in quasar evolution where the obscuring dusty gas is driven out by the quasar^{17,18,19}. To test this, we have studied a sample of fourteen Type 1 quasar hosts at $z > 1$ with carbon-monoxide (CO) molecular line measurements at rotational level transition $J_{\text{up}} \geq 7$. Radiative transfer modelling of CO line emission from AGN hosts suggests that such high excitation molecular gas must be heated by the AGN radiation field because gas temperatures in star-forming regions are not high enough to produce their observed luminosities^{20,21}. The resolved sizes of these line emitting regions are $\lesssim 1$ kpc²², so they can be linked directly to ongoing energy and momentum release by the quasar. We use data from

29 the literature and any relevant data in the Atacama Large sub-Millimetre Array (ALMA) archive with
30 sub-arcsecond imaging to confirm that the line emission is associated with the quasar. We performed
31 broad-band SED fitting (see Methods) to infer host galaxy star formation rate (SFR), bolometric AGN
32 luminosity (L_{AGN}) and quasar extinction ($E_{\text{B-V}}$), and obtained black hole masses from the literature
33 to infer the Eddington ratios (see Methods).

34 We find that red quasars ($E_{\text{B-V}} > 0.25^{15}$) have larger $J_{\text{up}} \geq 7$ CO line widths by a factor of ≈ 3
35 when compared to blue quasars (see Fig. 1). They also inhabit a different region of parameter space
36 with respect to [CI] or [CII] line widths, which primarily trace gas in the disc of the host galaxy, but
37 have similar SFR, black hole mass and AGN luminosity to the non-red quasars. Therefore, the larger
38 CO line widths of the red quasars cannot be explained by stronger stellar feedback, higher dynamical
39 mass or galaxy geometry (see Fig 1 and Methods), and we conclude that these are associated with
40 quasar-driven molecular outflows with velocities of 700–1000 km s⁻¹. Two of the three red quasars in
41 our sample do not appear in the NRAO VLA Sky Survey or the VLA FIRST Survey, indicating the
42 absence of powerful radio jets and jet-mode feedback.

43 Two of the three red quasars in our sample (MG J0414+0534 and ULAS J1234+0907) show an excess
44 of emission at around 3 μm relative to the SED model, while none of the non-red quasars show this
45 feature. This feature is predicted by theoretical models to be produced by thermal emission from hot
46 dust close to the quasar sublimation radius^{17,23}. Additionally, the CO emission from the two lensed red
47 quasars in the sample (MG J0414+0534 and J1042+1641) have been resolved and found to be ~ 100 pc
48 in size (see Methods), consistent with the expected sizes of CO line emitting regions for molecular gas
49 penetrated by strong X-ray radiation fields^{24,25}. This confirms that the outflows we detect are within
50 the stellar bulge ($\lesssim 1$ kpc), but extend beyond the region dominated by the gravity of the black holes
51 (5–10 pc).

52 In order to drive an outflow, AGN radiation pressure has to overcome the inward gravitational pull
53 of the interstellar medium (ISM) of the host galaxy. The balance of these two forces defines an
54 ‘effective Eddington limit’¹⁰ above which the ISM should be expelled. By relating dust extinction to
55 column density, we show that all three red quasars lie in a ‘forbidden zone’ on the column density
56 (N_{H}) – Eddington ratio (λ_{Edd}) plane¹¹ (see Methods); this further supports that radiation pressure

57 is responsible for these outflows (Fig. 2). In contrast, the non-red quasars populate a region of
58 the parameter space where the nucleus is unobscured, suggesting that they have already driven out
59 their surrounding gas. Assuming a spherical model for the outflows, we infer outflow timescales of
60 ≈ 0.05 Myr (see Methods), which are within the expected timescale of a radiatively-driven blow-
61 out^{11,26}. We test an alternative scenario where the outflows are powered by an accretion disc wind,
62 but find that this mechanism is unlikely to explain the outflow velocities (see Methods). Furthermore,
63 we find that several other objects that are known to have ultra-fast outflows or broad absorption lines
64 do not show evidence of molecular outflows (Fig. 2) demonstrating that the presence of dust is a better
65 predictor of outflows than relativistic winds.

66 It has been speculated that molecules are destroyed in more energetic systems such that the outflowing
67 gas is primarily ionised²⁷. Our results show that molecules can survive in outflows, even from the
68 brightest quasars ($L_{\text{AGN}} > 10^{48}$ ergs s⁻¹). These outflows have velocities comparable to the maximum
69 outflow velocities of ionised gas for quasars with $L_{\text{AGN}} \sim 10^{47}$ – 10^{48} ergs s⁻¹²⁷, and are consistent
70 with the average outflow velocity traced by the [CII] line for one of the non-red quasars in the sample
71 (600–1000 km s⁻¹ over radii of 1–5 kpc¹³). This suggests that the molecular outflow velocities are
72 maintained as the outflow expands out of the galaxy (~ 10 kpc) where the cold outflow may either
73 stall or be destroyed, transitioning to a purely ionised phase, as predicted by radiation-hydrodynamical
74 simulations^{12,28}.

75 State-of-the-art cosmological simulations and semi-analytic models of galaxy evolution unanimously
76 require strong AGN feedback in order to explain the observed properties of massive galaxies across
77 cosmic time^{1,2,3,4}. However, whether AGN feedback operates predominantly via bulk ejection of the
78 ISM or via prevention of cooling has remained an open question. We have demonstrated that quasar
79 blow-out is effective at removing the fuel for star formation during the cosmic peak of galaxy growth,
80 supporting an ejective feedback scenario. Due to the short outflow timescales (0.05 Myr) we are able
81 to associate the outflows with the ongoing energy output of the quasar into the stellar bulge, finding
82 excellent agreement with models of radiative feedback. These results indicate that radiative AGN
83 feedback is the physical driver of scaling relations between galaxies and their central supermassive
84 black holes²⁹.

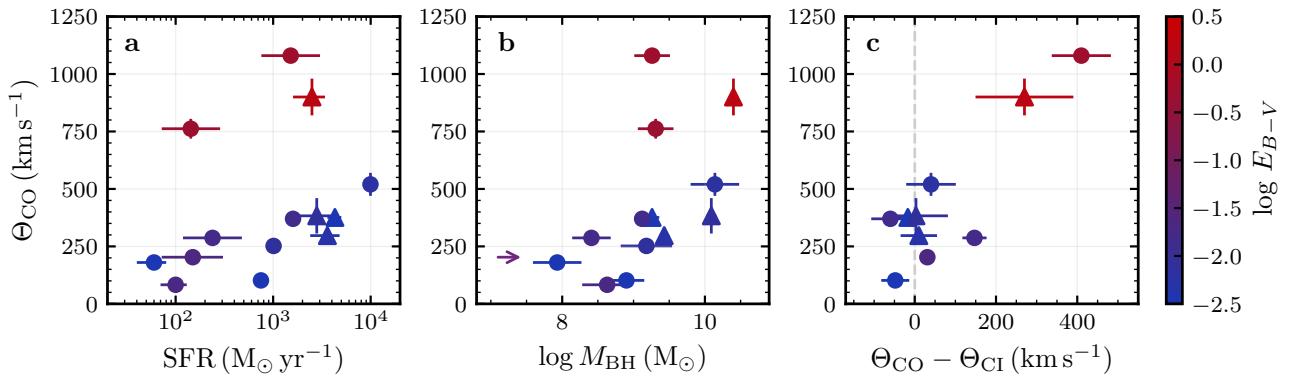


Figure 1: **Comparison of CO line widths of the sample with reddening.** **a:** $J_{\text{up}} > 7$ CO FWHM against SFR (lensing-corrected). **b:** CO FWHM against M_{BH} (lensing-corrected). **c:** difference in CO and [CI] or [CII] FWHM (as a proxy for galaxy dynamical mass) against CO FWHM. The circles identify the sources that are lensed. The colour scale indicates quasar extinction (E_{B-V}). The red quasars inhabit a different parameter space than the blue quasars, which follow expected trends with dynamical mass (see Methods).

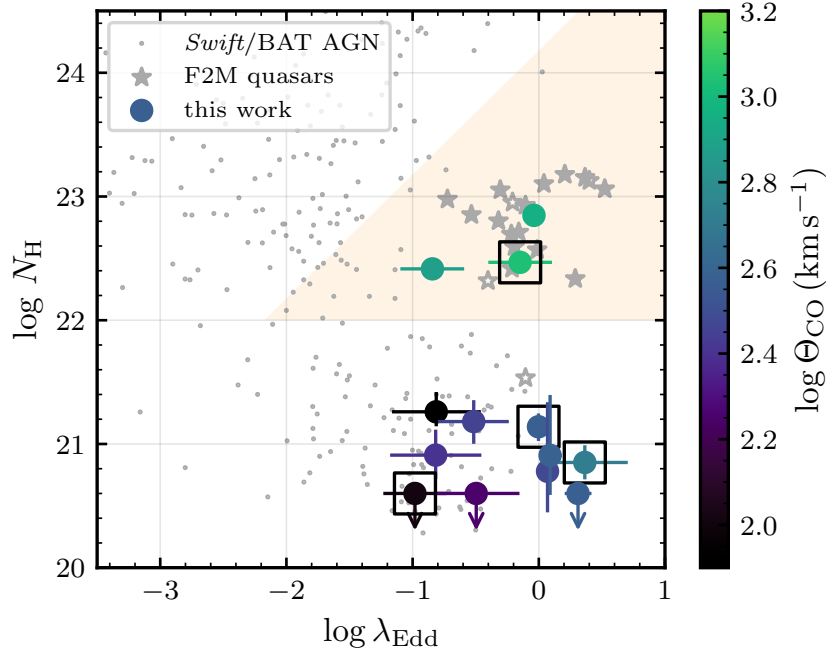


Figure 2: **Eddington ratio against gas column density.** The shaded region identifies the ‘forbidden zone’ where radiation pressure on dust is sufficient to expel the obscuring column density¹¹ (see Methods). We convert dust-reddening (E_{B-V}) to gas column density (N_H)³⁰, assuming that the molecular gas is a good approximation for the total gas column density. We cannot reliably constrain E_{B-V} at values below 0.01, so adopt this as an upper limit for the equivalent column density. Boxes identify the objects in our sample where ultra-fast outflows or broad absorption lines have been detected³¹. The stars show quasars from F2M surveys ($0.1 < E_{B-V} < 2.5$) where N_H is inferred from E_{B-V} (filled stars) or X-ray spectra (open stars)³². The dots are X-ray detected AGN in the *Swift*/BAT sample³³, where N_H is inferred from X-ray spectra. The red quasars are in the forbidden zone where radiative pressure can drive out the obscuring gas, indicating that radiation pressure is responsible for the outflows.

85 **Methods**

86 **ALMA observations**

87 In addition to CO, [CI] and [CII] measurements obtained from the literature, we present new ALMA
88 data for several objects. These observations are summarised in Table 1. Where we observe the
89 CO (7–6) lines we also observe the [CI] (2–1) line simultaneously. Each data set was calibrated and
90 reduced using the ALMA pipeline in CASA³⁴. The calibrated data were inspected to confirm the
91 quality of the pipeline calibration. We self-calibrated the data for SDSS J0248+1913 and
92 SDSS J1330+1810 using the continuum-only spectral windows with a single solution interval for
93 each antenna in both amplitude and phase. For MG J0414+0534, we performed phase calibration
94 with a solution interval of 240 seconds.

95 We created a clean image cube of the spectral window containing the line emission with natural
96 weighting of the visibilities (Fig. 3) and extracted a spectrum in an aperture around the lens. The line
97 profiles (presented here and where taken from the literature) do not show asymmetries that would
98 indicate that their shapes are strongly affected by differential magnification.

99 To measure the line FWHM, we fit the line profiles with a single Gaussian. For MG J0414+0534, the
100 CO (7–6) line is so broad that it is blended with the [CI] (2–1) line (Fig. 4c). We fit Gaussians to both
101 lines simultaneously with the systemic redshift fixed to the value found for the CO (3–2)³⁵. For
102 SDSS J1330+1810, part of the [CI] line falls outside the spectral window. For these two cases, the
103 integrated line luminosity is estimated from the fitted Gaussian profile rather than directly from the
104 image. The line profiles and Gaussian fits for these ALMA observations are shown in Fig. 4.

105 **AGN luminosity, extinction and black hole masses**

106 We use AGNFITTER³⁶ to fit the broad-band SED of each quasar and host galaxy (Fig. 5). This
107 software includes accretion disc, torus, host galaxy and starburst templates^{17,36}. The accretion disc
108 component is reddened by an extinction model³⁷ parameterised by rest-frame E_{B-V} . We compile
109 photometry from all-sky surveys, where available, or from the literature.

110 We assume a minimum uncertainty of 10 percent on photometric measurements to allow for source
111 variability and microlensing effects. Although the photometry will be blended with light from the

112 lensing galaxy, the quasar point-source emission strongly dominates the emission. This is evident
 113 from the available ultra-violet–infrared imaging with the Hubble Space Telescope (HST), e.g. in the
 114 CfA-Arizona Space Telescope Lens Survey³⁸. The host galaxy emission can be fit in only a few
 115 cases, for most only accretion disc and torus components are constrained.

116 Following previous work¹⁷, we calculate the bolometric AGN luminosity (L_{AGN}) by integrating the
 117 quasar accretion disc model (‘big blue bump’) in the range 0.05–1 μm with an additive correction of
 118 0.3 dex to account for X-ray emission not included in the model fit, i.e.

$$\log L_{\text{AGN}} = \log L_{0.05-1\mu\text{m}} + 0.3 - \log \mu_{\text{qso}}, \quad (1)$$

119 where μ_{qso} is the quasar magnification. We assume black hole mass (M_{BH}) estimates from the
 120 literature that were derived using the virial method. For consistency, we adopt the same quasar
 121 lensing magnification used for the black hole mass to infer the intrinsic bolometric AGN luminosity.

122 **Star formation rates**

123 Where possible, we obtain far-infrared luminosities from the literature. While AGNFITTER includes
 124 templates to fit the host galaxy dust emission, these models are empirically derived from low-redshift
 125 starbursts and may not be appropriate for high-redshift quasar hosts. Indeed, we found that the
 126 far-infrared–mm spectra are often poorly fit by these templates. Instead, we adopt far-infrared
 127 luminosities taken from the literature, most of which were calculated with free-form models. Where
 128 there is insufficient photometry to fit a dust model, we assume an optically-thin modified black-body
 129 with the median effective dust temperature and emissivity found for a large sample of quasar hosts³⁹.
 130 While the effective dust temperature may be quite different depending on the choice of model, the
 131 total infrared luminosity will be similar as it is constrained by the photometry.

132 We convert far-infrared luminosity to total infrared luminosity (8–1000 μm) using the
 133 colour-correction factor⁴⁰ of 1.91 and to a dust-obscured SFR using a standard calibration⁴¹
 134 assuming a Salpeter initial mass function.

135 The intrinsic SFR for some of the lensed sources have previously been inferred from lens modelling
 136 of ALMA observations of sub-mm dust emission²². For APM 08279+5255, we adopt the CO

137 magnification factor from lens modelling in literature to infer a SFR from the uncorrected
138 measurement⁴². For other lensed sources, we assume a sub-mm magnification factor of 10_{-5}^{+10} in line
139 with typical values for four-image lensed quasar systems²² to infer the SFR. All values and references
140 are given in Table 2.

141 Note that the sub-mm magnification is not the same as the quasar magnification, as these will be
142 lensed differently depending on the size and location of the emitting region. We did not check for
143 consistency between the lens models used to obtain black hole masses from the literature and those
144 used to obtain the SFR, but we do not compare these properties.

145 **Comparison of CO line dynamics**

146 Details of the line properties, SFR, black hole masses, E_{B-V} , AGN luminosities and literature
147 references for the sample of quasars is presented in Table 2. The sample probes 2, 3 and 4 orders of
148 magnitude in SFR, black hole mass and AGN luminosity, respectively.

149 The sample probes a range of CO rotational transitions, $J_{\text{up}} = 7-11$. The kinematics of these
150 high-excitation CO lines have not yet been systematically studied at high redshift so little is known
151 about their typical dynamics. However, we are able to compare the CO (7–6) and CO (11–10) line
152 widths for MG J0414+0534 and find comparably large values (Table 2)[†]. These lines are both
153 significantly broader than the 580 km s^{-1} found for the CO (3–2) line³⁵ in the same system,
154 suggesting the CO (7–6) has similar dynamics to higher excitation lines.

155 For the non-red quasars, we find positive correlations between CO FWHM and SFR ($p = 0.004$) and
156 between CO FWHM and black hole mass ($p = 0.00001$). While Pearson correlation tests may not be
157 accurate when considering such small sample sizes, these correlations can be explained by
158 well-understood physical phenomena. The correlation with SFR (Fig. 1, top) could reflect increased
159 turbulence due to radiative stellar winds or supernovae: gas dispersion of up to 100 km s^{-1} can be
160 induced by stellar feedback in regions of Eddington-limited star formation^{43,44}. Alternatively, it may
161 reflect the relationship between SFR and dynamical mass. The correlation between FWHM and
162 black hole mass (Fig. 1, middle) may reflect a larger dynamical mass as expected from canonical
163 scaling relations between black hole mass and stellar mass²⁹. These are expected correlations found

[†]The FWHM of the CO (11–10) line is shown for MG J0414+0534 in all plots

164 for [CII] in quasar host galaxies⁴⁵, although these have not been previously investigated for these
165 high-excitation CO lines. The red quasars do not follow the correlations observed by the non-red
166 quasars, which follow expected trends with dynamical mass, and there appears to be no significant
167 correlation between SFR or black hole mass and reddening ($p = 0.45$ and $p = 0.24$, respectively, for
168 the whole sample).

169 We also compare the high-excitation CO with [CI] or [CII] line profiles to further test whether the CO
170 lines are associated with the host galaxy disc dynamics or inclination. [CI] and [CII] trace gas at
171 lower temperatures and densities, but also CO-dark molecular gas⁴⁶, so they probe the galaxy at
172 larger disc radii (i.e. maximum circular velocity)^{45,47,48}. Fig. 1 (bottom) shows the CO FWHM
173 against its difference from the [CI] or [CII] line FWHM for the sources with such measurements. The
174 CO and [CI] or [CII] line FWHMs are similar for the blue quasars, so these lines could both relate to
175 gas in the host galaxy. However, the red quasars have CO FWHMs 300–400 km s⁻¹ larger than their
176 [CI] or [CII] line widths, indicating that the CO is not primarily from rotating gas in the disc.

177 Therefore, we conclude that outflows are the most likely explanation for the CO large linewidths.
178 Using an orthogonal distance regression, we fit a linear relationship between CO FWHM and SFR for
179 the non-red quasars. Assuming the line profiles have contributions from both outflows and host
180 galaxy which can be described by Gaussians of equal height, we estimate a line-of-sight outflow
181 velocity of 1030 ± 80 , 750 ± 50 and 820 ± 140 km s⁻¹ for MG J0414+0534, J1042+1641 and
182 ULAS J1234+0907, respectively. These velocities may be intrinsically larger depending on the
183 geometry of the outflows.

184 As we show in Figs. 2 and 6, there is no indication that the red quasars in our sample have larger
185 AGN luminosities or larger Eddington ratios than the non-red quasars (although this may not be true
186 for the populations in a statistical sense⁴⁹).

187 **Radiatively-driven outflows**

188 The abundance of dust is conducive to strong quasar feedback. By enhancing the absorption cross
189 section to ultra-violet and optical AGN radiation, the dusty ISM can, in principle, be driven out by
190 radiation pressure^{10,11}. The balance of these two forces defines an ‘effective Eddington limit’¹⁰

191 above which the ISM can be expelled, resulting in correlations between galaxy bulge properties and
 192 black hole mass that are in agreement with observations⁵⁰.

193 Recent radiation-hydrodynamic simulations^{12,28,51} predict that radiation pressure operates and
 194 launches outflows from < 1 kpc scales, which shock-heat and generate hot, over-pressurised bubbles
 195 on larger scales⁵² thereby reducing the supply of gas for star formation in the inner region of the
 196 galaxy. This blow-out phase is likely short-lived because outflows propagate on a characteristic
 197 timescale of

$$t_{\text{out}} \sim 1 (R_{\text{out}}/\text{kpc}) \left(v_{\text{out}}/1000 \text{ km s}^{-1} \right)^{-1} \text{ Myr.} \quad (2)$$

198 For this reason, we expect quasars to be below the effective Eddington limit unless their host galaxies
 199 are experiencing a powerful outflow. This limit creates a ‘forbidden zone’ on the $\lambda_{\text{Edd}}-N_{\text{H}}$ plane in
 200 the regime where the dust is optically thick to ultra-violet radiation which can approximated by

$$N_{\text{H}} \sim \frac{\lambda_{\text{Edd}}/\sigma_{\text{T}}}{1 - \frac{\kappa_{\text{IR}}}{\kappa_{\text{T}}} \lambda_{\text{Edd}}}, \quad (3)$$

201 where σ_{T} is the Thompson cross-section, κ_{T} is the electron scattering opacity and κ_{IR} is the dust
 202 opacity¹¹. Previous studies^{11,53} have defined lower limits for the forbidden zone of $10^{21.5}-10^{22} \text{ cm}^{-2}$
 203 where column densities could be associated with diffuse cold gas in the galaxy: we have adopted the
 204 more conservative assumption of 10^{22} cm^{-2} , although the choice does not affect our interpretation.

205 Two red quasars in our sample have measured sizes of their CO emission from lens modelling in the
 206 literature⁵⁴ and this work (Fig. 7). From Eq. 2, we estimate an outflow timescale of ≈ 0.05 Myr for
 207 MG J0414+0534 and J1042+1641.

208 **Test of an energy-driven scenario**

209 Fig. 2 supports the scenario that radiation pressure drives the observed outflows. However, outflows
 210 may also be ‘energy-driven’ by high-velocity winds produced near the accretion disc^{6,52,55,56}.

211 Ultra-fast outflows have been detected in X-ray spectra of high-redshift quasars⁵⁷ including the red
 212 quasar MG J0414+0534, which contains an ultra-fast outflow with velocity $0.3c$ ⁵⁸ that could
 213 potentially power the observed molecular outflow. The kinematics of the wind is a key factor to
 214 discriminate between the two scenarios: the momentum flux for energy-driven outflows is expected

215 to be $\dot{p} \sim v_{\text{out}}/v_{\text{UFO}} \gtrsim 100 L_{\text{AGN}}/c$, compared to $\dot{p} \sim L_{\text{AGN}}/c$ for momentum or radiation
 216 pressure-driven winds¹². For the inferred $L_{\text{AGN}} = 10^{47.2}$ ergs s⁻¹, we predict an energy-driven mass
 217 outflow rate ($\dot{M} = \dot{p}/v_{\text{out}}$) of $\approx 10^6 M_{\odot} \text{ yr}^{-1}$ for the gas probed by the CO (11–10). Adopting a
 218 simple spherical model for the molecular outflow with radius of $\approx 50 \text{ pc}^{54}$ and velocity 1000 km s^{-1} ,
 219 the implied outflow timescale is $\approx 0.05 \text{ Myr}$ and thus its total mass is $\approx 10^{10} M_{\odot}$. Adopting the 3σ
 220 upper limit for non-detection of CO (1–0)⁵⁹, a typical CO-to-H₂ conversion factor of $0.8 \text{ K km s}^{-1} \text{ pc}^2$
 221 and typical³⁹ magnification factor of 10, the molecular gas mass in the host galaxy is $< 10^{9.5} M_{\odot}$.
 222 Therefore, for an energy-driven wind model, the gas in the outflow from MG J0414+0534 would be
 223 more than twice as massive as the molecular gas in the disc: an unlikely scenario given the high SFR
 224 (Table 2) and the massive molecular gas reservoirs of quasar hosts that are similar to normal
 225 starbursts^{59,60,61}. This disfavours an energy-driven scenario for this object, implying that an accretion
 226 disc wind must couple very inefficiently with the ISM in order to produce the outflow we observe.

227 **Acknowledgements**

228 This research used SciPy, NumPy and Matplotlib packages for Python^{62,63,64}, and also the
229 NASA/IPAC Extragalactic Database (NED), SIMBAD⁶⁵ and VizieR⁶⁶ catalogue access tools. We
230 made use of ALMA data with project codes 2018.1.01008.S, 2019.1.00948.S and 2019.1.00964.S.
231 ALMA is a partnership of ESO (representing its member states), NSF (USA) and NINS (Japan),
232 together with NRC (Canada), MOST and ASIAA (Taiwan), and KASI (Republic of Korea), in
233 cooperation with the Republic of Chile. The Joint ALMA Observatory is operated by ESO,
234 AUI/NRAO and NAOJ.

235 **Data Availability**

236 All observations reported in this work are publicly available in the ALMA archive
237 (<https://almascience.eso.org/aq>). The data sets generated during the current study are
238 available from the corresponding author on reasonable request.

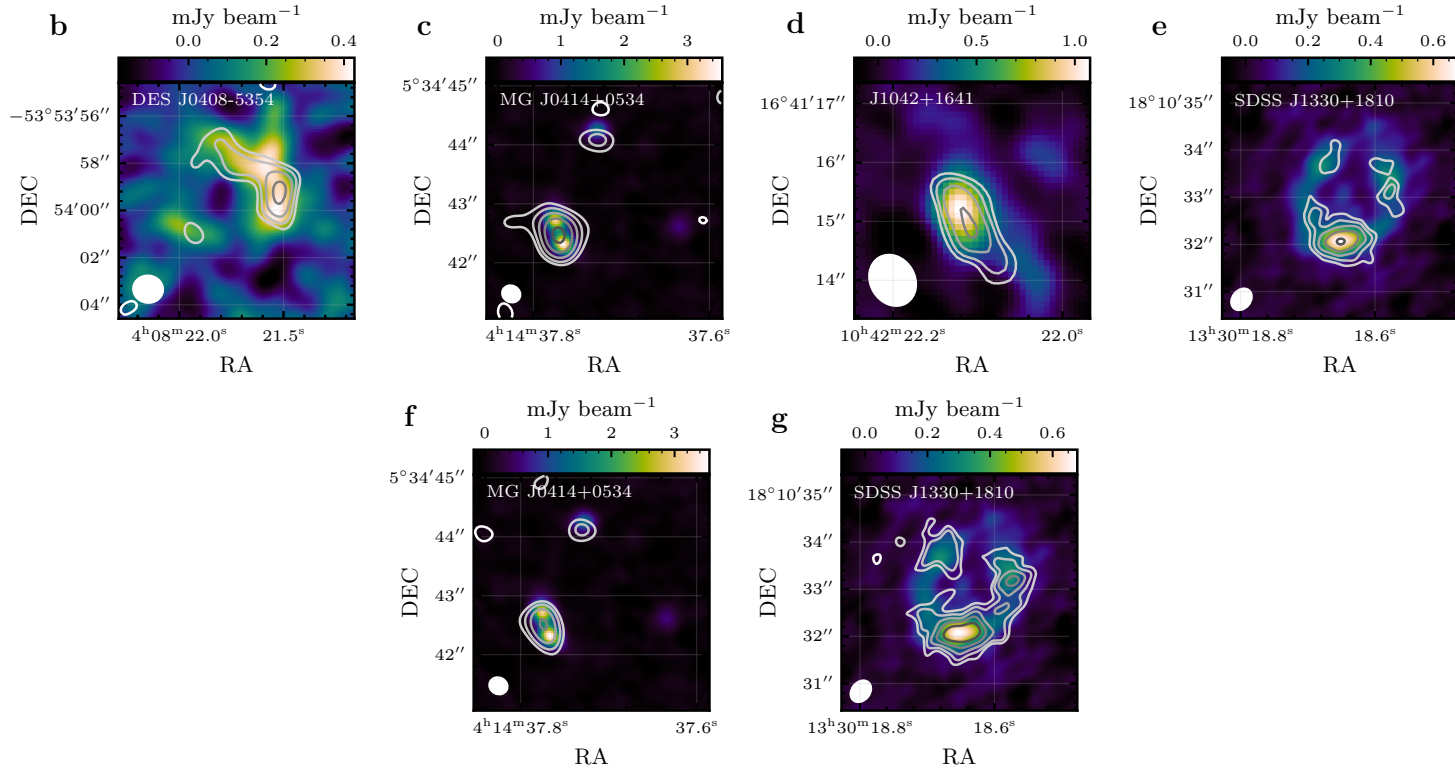


Figure 3: **ALMA imaging for the new data presented in this work.** **a-d:** the sub-mm continuum emission with contours of the velocity-integrated CO line emission in signal-to-noise intervals of $-3, 3, 3\sqrt{2}, 6, 6\sqrt{2}, \dots$ etc. The synthesised beam is shown by the ellipse in the lower-left corner. **e,f:** the same for the [CI] line emission.

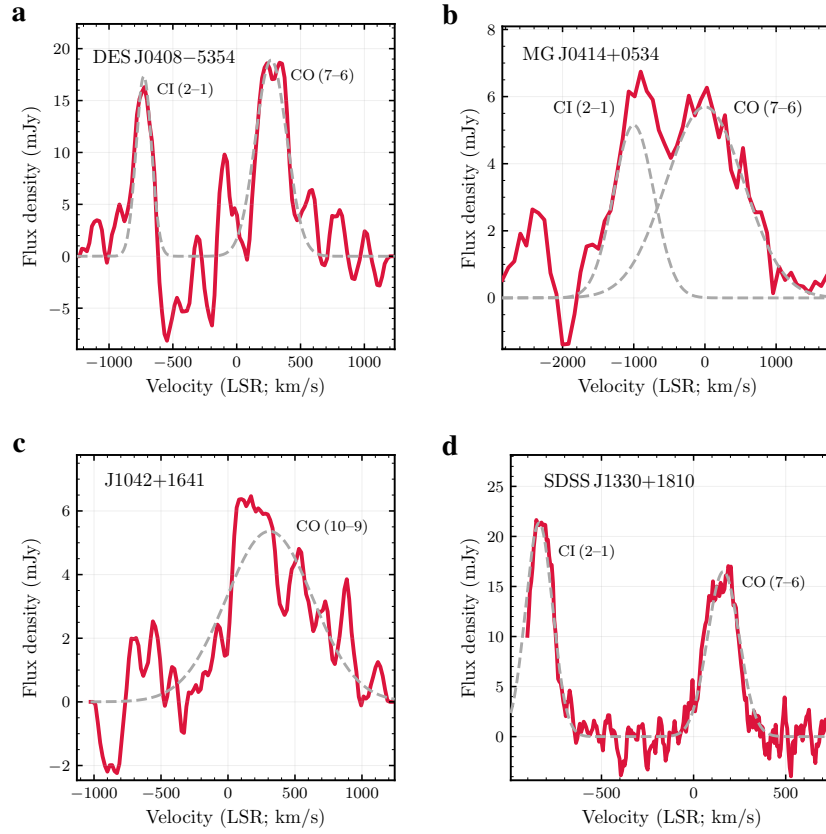


Figure 4: **Line profiles for the new data presented in this work.** The spatially-integrated line profiles (red line) and Gaussian fits to the CO and [CI] line emission (grey dashed line). For all except MG J0414+0534 (c), the systemic redshift is based on optical spectroscopy so a velocity offset in the CO could be because the ionic lines trace out-flowing gas.

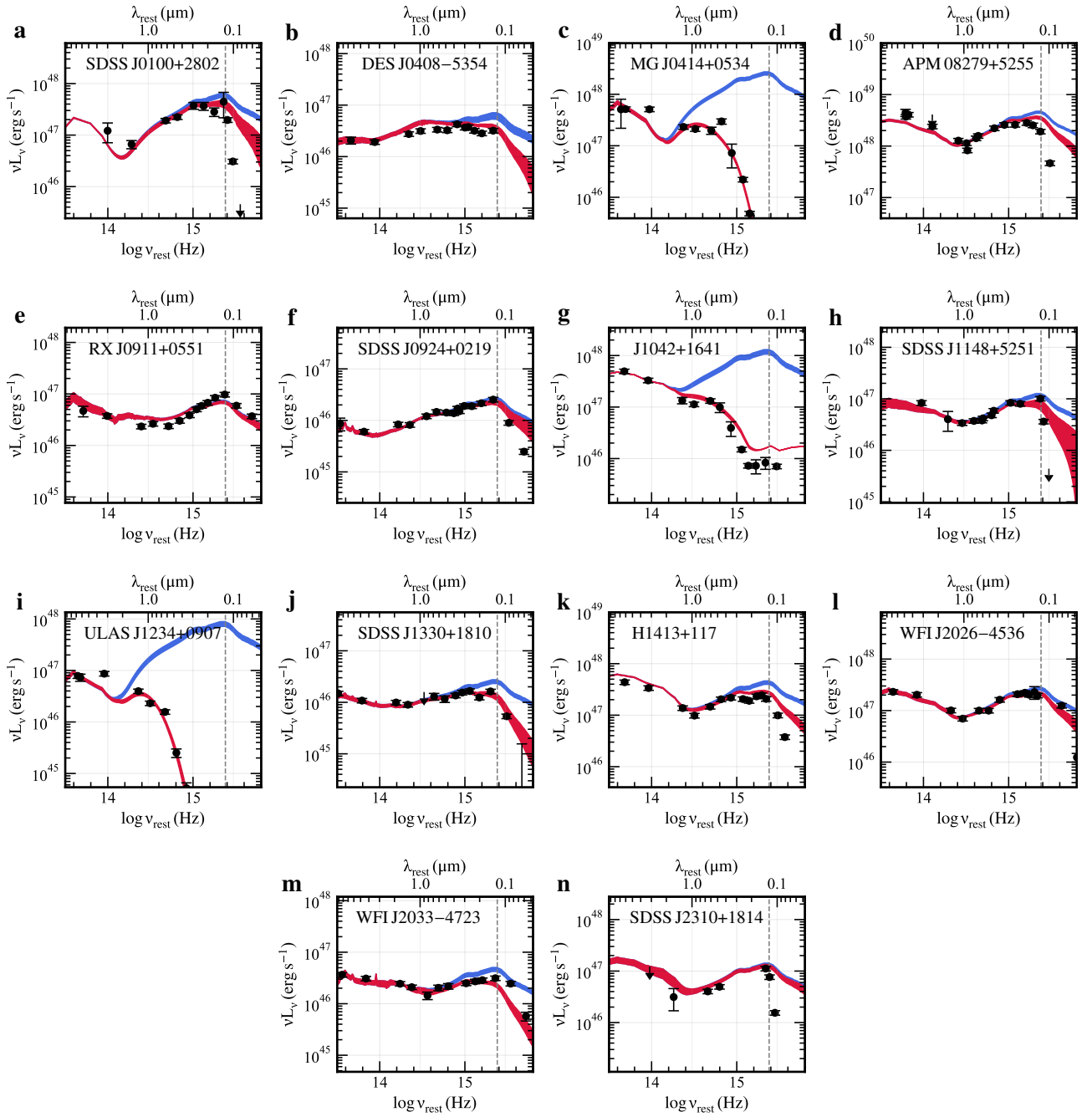


Figure 5: **SED fits for the quasar sample.** We use AGNFitter³⁶ to fit broad-band SEDs from the ultra-violet to mid-infrared. The red curve is a solid fill between 16th to 86th percentiles of the models from the MCMC analysis. The blue curve shows the quasar models without dust attenuation. The grey dashed line is the rest-frame frequency of Lyman- α ; photometric measurements at or above this frequency are ignored because they are affected by absorption by the intergalactic medium.

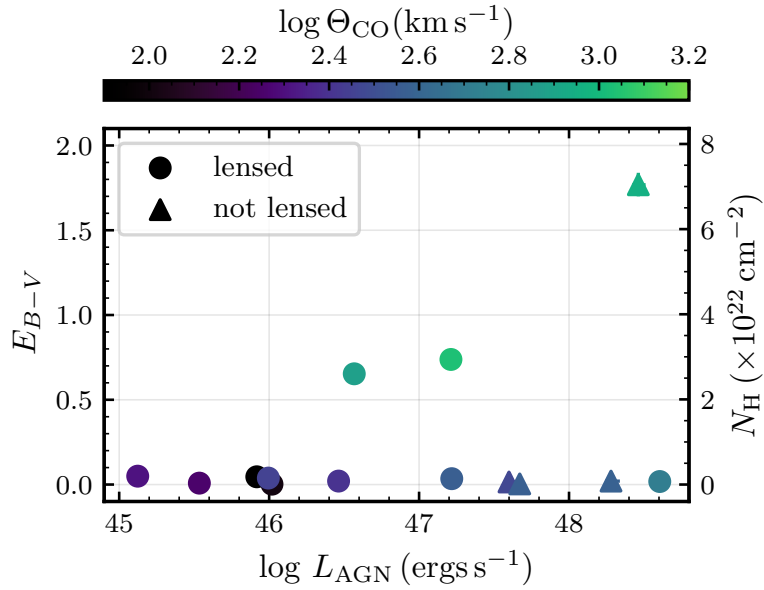


Figure 6: **Reddening against bolometric AGN luminosity (lensing-corrected)**. The opposing y-axis shows the corresponding column density³⁰. Circles identify sources that are lensed. Outflows are observed even for AGN luminosities $> 10^{48}$ ergs s^{-1} .

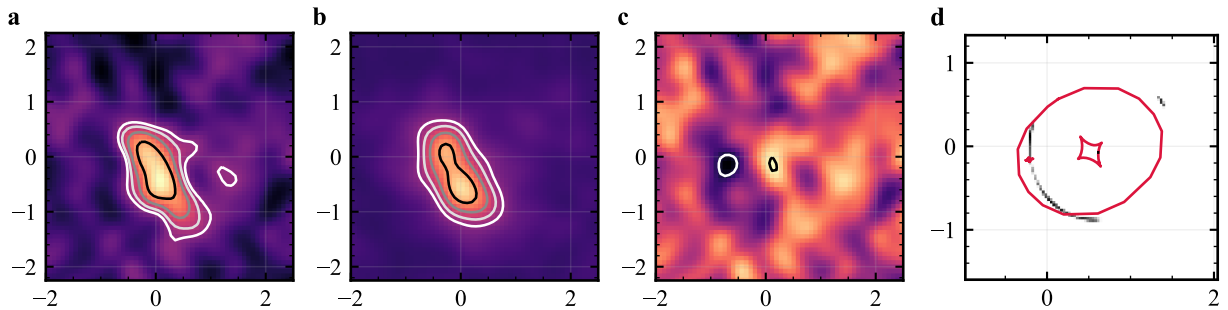


Figure 7: **Lens modelling of J1042+1641**. We use `VISILENS`^{67,68} to model the integrated CO (10–9) emission. We adopt the fiducial lens model from the literature¹⁵ consisting of a singular isothermal ellipsoid for the main lens, an isothermal sphere for the satellite galaxy and external shear. The source is modelled as a circular Gaussian with size, position and flux density as free parameters. We find a best-fit FWHM of 70 ± 10 pc. **a–c**: The dirty image of the data, dirty image of the model and residual image. The contours are in signal-to-noise ratio intervals of $-3, 3, 3\sqrt{2}, 6, 6\sqrt{2}$. **d**: The source and lens model (grey; log-scale) and lensing caustics (red).

Project	Name	Line(s)	Θ_{beam} (arcsec)	ν_{cont} (GHz)	S_{ν} (mJy)	I_{line} (Jy km s ⁻¹)
2018.1.01008.S	MG J0414+0534	CO (7–6); [CI] (2–1)	$0.3 \times 0.3^{\dagger}$	236	10.1 ± 0.4	7.8*; 3.7*
2019.1.00948.S	SDSS J1330+1810	CO (7–6); [CI] (2–1)	0.5×0.4	342	6.3 ± 0.2	3.5 ± 0.2 ; 3.9*
2019.1.00964.S	DES J0408–5354	CO (7–6); [CI] (2–1)	$1.2 \times 1.1^{\dagger}$	247	3.0 ± 0.4	4.9 ± 0.7 ; 3.3 ± 0.5
	J1042+1641	CO (10–9)	0.9×0.7	256	2.0 ± 0.3	4.0 ± 0.7

Table 1: **New ALMA observations presented in this work.** We give the project code, the synthesised beam FWHM (Θ_{FWHM}) used to extract the line profile and continuum flux density, the continuum frequency (ν_{cont}), the continuum flux density (S_{ν}), the integrated line intensity (I_{CO}) and line systemic redshift (z_{CO}) based on a Gaussian fit to the line profile. \dagger denotes cases where we have applied a uv taper to the data weights to improve surface brightness sensitivity. *For these cases, the line intensity is approximated from the Gaussian fit to the line profile (see Methods).

Name	N_{im}	z_s	Line	Θ_{line} (km s^{-1})	SFR ($M_{\odot} \text{ yr}^{-1}$)	$\log M_{\text{BH}}$ (M_{\odot})	E_{B-V}	$\log L_{0.05-1\mu\text{m}}$ (ergs s^{-1})	μ_{qso}	References
DES J0408–5354	4	2.375	CO (7–6)	290 ± 20	240^{+240}_{-120}	8.41 ± 0.27	$0.038^{+0.015}_{-0.016}$	$47.04^{+0.07}_{-0.08}$	22	⁶⁹ , this work
			[CI] (2–1)	140 ± 20						This work
MG J0414+0534	4	2.64	CO (11–10)	1080 ± 20	1500^{+1500}_{-800}	9.26	$0.738^{+0.017}_{-0.014}$	$48.66^{+0.04}_{-0.03}$	56.4	39,70,71
			CO (7–6)	1280 ± 110						This work
			[CI] (2–1)	670 ± 70						This work
APM 08279+5255	4	3.91	CO (11–10)	520 ± 50	10000 ± 200	10.0	$0.018^{+0.006}_{-0.006}$	$48.91^{+0.01}_{-0.02}$	4	20,39
RX J0911+0551	4	2.79	CO (11–10)	100 ± 30	750 ± 50	8.9	$0.002^{+0.005}_{-0.002}$	$47.10^{+0.02}_{-0.02}$	17.5	22,70,72
SDSS J0924+0219	4	1.525	CO (8–7)	180 ± 10	60 ± 20	7.93 ± 0.35	$0.008^{+0.012}_{-0.006}$	$46.65^{+0.04}_{-0.02}$	26.2	73
J1042+1641	4	2.25	CO (10–9)	760 ± 40	140^{+140}_{-70}	9.31 ± 0.25	$0.65^{+0.02}_{-0.02}$	$48.34^{+0.02}_{-0.05}$	117	⁷⁴ , this work
SDSS J1330+1810	4	1.39	CO (7–6)	203 ± 6	150^{+160}_{-80}	-	$0.05^{+0.01}_{-0.02}$	$46.66^{+0.04}_{-0.04}$	68.2	39,70, this work
			[CI] (2–1)	172 ± 6						This work
H1413+117	4	2.56	CO (9–8)	370 ± 10	1600 ± 60	9.12 ± 0.01	$0.06^{+0.06}_{-0.02}$	$47.93^{+0.04}_{-0.04}$	10.3	22,73
WFIJ2026–4536	4	2.23	CO (10–9)	252 ± 7	1010 ± 60	9.18 ± 0.36	$0.02^{+0.01}_{-0.01}$	$47.68^{+0.04}_{-0.02}$	33.0	22,75,76
WFIJ2033–4723	4	1.66	CO (8–7)	80 ± 10	100 ± 30	8.63 ± 0.35	$0.03^{+0.05}_{-0.03}$	$47.08^{+0.06}_{-0.04}$	19.7	22,73,77
SDSS J0100+2802	1	6.33	CO (10–9)	380^{\ddagger}	2800 ± 1400	10.09 ± 0.07	$0.02^{+0.02}_{-0.01}$	$47.98^{+0.06}_{-0.04}$	-	78,79
			[CII]	380 ± 20						79
SDSS J1148+5251	1	6.42	CO (7–6)	300 ± 40	3600 ± 1200	9.43 ± 0.07	$0.02^{+0.02}_{-0.01}$	$47.30^{+0.04}_{-0.03}$	-	80,81,82
			[CII]	287 ± 28						83
ULAS J1234+0907	1	2.50	CO (7–6)	900 ± 80	2500 ± 900	10.4	$1.77^{+0.07}_{-0.07}$	$48.16^{+0.05}_{-0.04}$	-	84,85
			[CI] (2–1)	630 ± 90						85
SDSS J2310+1814	1	6.00	CO (9–8)	380 ± 20	4300 ± 700	9.6	$0.004^{+0.007}_{-0.003}$	$47.37^{+0.04}_{-0.03}$	-	80,86,87
			[CII]	390 ± 20						86

Table 2: **Summary of the objects in the sample.** We give the number of lensed quasar images ($N_{\text{im}} = 1$ if not strongly lensed), source redshift (z_s), CO line transition (or other line), line FWHM from a single Gaussian fit to the line profile, SFR (lensing-corrected), black hole mass (M_{BH}), extinction (E_{B-V}), integrated luminosity of the BBB template ($\log L_{0.05-1\mu\text{m}}$, not lensing-corrected) and assumed value of the quasar magnification from the literature (μ_{qso}). Where no uncertainty was given for the black hole mass, we assume an uncertainty of 0.25 dex which is the typical scatter found for black hole scaling relations. For SDSS J1330+1810, line widths have not been reported, so we infer a lower limit the black hole mass from the AGN bolometric luminosity assuming Eddington-limited accretion. References given are for the line FWHM, black hole mass and quasar magnification, and photometry used for the optical–infrared SED fitting (if not from all-sky catalogues).

References

- [1] Di Matteo, T., Springel, V. & Hernquist, L. Energy input from quasars regulates the growth and activity of black holes and their host galaxies. *Nature* **433**, 604–607 (2005). astro-ph/0502199.
- [2] Somerville, R. S. & Davé, R. Physical Models of Galaxy Formation in a Cosmological Framework. *ARA&A* **53**, 51–113 (2015). 1412.2712.
- [3] Schaye, J. *et al.* The EAGLE project: simulating the evolution and assembly of galaxies and their environments. *MNRAS* **446**, 521–554 (2015). 1407.7040.
- [4] Weinberger, R. *et al.* Simulating galaxy formation with black hole driven thermal and kinetic feedback. *MNRAS* **465**, 3291–3308 (2017). 1607.03486.
- [5] King, A. The AGN-Starburst Connection, Galactic Superwinds, and $M_{BH}-\sigma$. *ApJL* **635**, L121–L123 (2005). astro-ph/0511034.
- [6] Costa, T., Sijacki, D. & Haehnelt, M. G. Feedback from active galactic nuclei: energy- versus momentum-driving. *MNRAS* **444**, 2355–2376 (2014). 1406.2691.
- [7] Förster Schreiber, N. M. & Wuyts, S. Star-Forming Galaxies at Cosmic Noon. *ARA&A* **58**, 661–725 (2020). 2010.10171.
- [8] Harrison, C. M. Impact of supermassive black hole growth on star formation. *Nature Astronomy* **1**, 0165 (2017). 1703.06889.
- [9] Harrison, C. M. *et al.* AGN outflows and feedback twenty years on. *Nature Astronomy* **2**, 198–205 (2018). 1802.10306.
- [10] Fabian, A. C., Vasudevan, R. V. & Gandhi, P. The effect of radiation pressure on dusty absorbing gas around active galactic nuclei. *MNRAS* **385**, L43–L47 (2008). 0712.0277.
- [11] Ishibashi, W., Fabian, A. C., Ricci, C. & Celotti, A. Revisiting the ‘forbidden’ region: AGN radiative feedback with radiation trapping. *MNRAS* **479**, 3335–3342 (2018). 1806.08387.

- 263 [12] Costa, T., Rosdahl, J., Sijacki, D. & Haehnelt, M. G. Quenching star formation with quasar
264 outflows launched by trapped IR radiation. *MNRAS* **479**, 2079–2111 (2018). 1709.08638.
- 265 [13] Cicone, C. *et al.* Very extended cold gas, star formation and outflows in the halo of a bright
266 quasar at $z > 6$. *A&A* **574**, A14 (2015). 1409.4418.
- 267 [14] Bischetti, M. *et al.* Widespread QSO-driven outflows in the early Universe. *A&A* **630**, A59
268 (2019). 1806.00786.
- 269 [15] Glikman, E. *et al.* Luminous WISE-selected Obscured, Unobscured, and Red Quasars in Stripe
270 82. *ApJ* **861**, 37 (2018). 1805.06961.
- 271 [16] Klindt, L., Alexander, D. M., Rosario, D. J., Lusso, E. & Fotopoulou, S. Fundamental
272 differences in the radio properties of red and blue quasars: evolution strongly favoured over
273 orientation. *MNRAS* **488**, 3109–3128 (2019). 1905.12108.
- 274 [17] Calistro Rivera, G. *et al.* The multiwavelength properties of red QSOs: Evidence for dusty
275 winds as the origin of QSO reddening. *A&A* **649**, A102 (2021). 2103.02610.
- 276 [18] Glikman, E. *et al.* FIRST-2MASS Red Quasars: Transitional Objects Emerging from the Dust.
277 *ApJ* **757**, 51 (2012). 1207.2175.
- 278 [19] Banerji, M., Alaghband-Zadeh, S., Hewett, P. C. & McMahon, R. G. Heavily reddened type 1
279 quasars at $z > 2$ - I. Evidence for significant obscured black hole growth at the highest quasar
280 luminosities. *MNRAS* **447**, 3368–3389 (2015). 1501.00815.
- 281 [20] Weiß, A. *et al.* Highly-excited CO emission in APM 08279+5255 at $z = 3.9$. *A&A* **467**,
282 955–969 (2007). astro-ph/0702669.
- 283 [21] van der Werf, P. P. *et al.* Black hole accretion and star formation as drivers of gas excitation and
284 chemistry in Markarian 231. *A&A* **518**, L42 (2010). 1005.2877.
- 285 [22] Stacey, H. R. *et al.* The rocky road to quiescence: compaction and quenching of quasar host
286 galaxies at $z \sim 2$. *MNRAS* **500**, 3667–3688 (2021). 2009.01277.

- 287 [23] Hönig, S. F. & Kishimoto, M. Dusty Winds in Active Galactic Nuclei: Reconciling
288 Observations with Models. *ApJL* **838**, L20 (2017). 1703.07781.
- 289 [24] Meijerink, R. & Spaans, M. Diagnostics of irradiated gas in galaxy nuclei. I. A far-ultraviolet
290 and X-ray dominated region code. *A&A* **436**, 397–409 (2005). astro-ph/0502454.
- 291 [25] Meijerink, R., Spaans, M. & Israel, F. P. Diagnostics of irradiated dense gas in galaxy nuclei. II.
292 A grid of XDR and PDR models. *A&A* **461**, 793–811 (2007). astro-ph/0610360.
- 293 [26] Ishibashi, W., Banerji, M. & Fabian, A. C. AGN radiative feedback in dusty quasar populations.
294 *MNRAS* **469**, 1496–1501 (2017). 1704.03712.
- 295 [27] Fiore, F. *et al.* AGN wind scaling relations and the co-evolution of black holes and galaxies.
296 *A&A* **601**, A143 (2017). 1702.04507.
- 297 [28] Costa, T., Rosdahl, J., Sijacki, D. & Haehnelt, M. G. Driving gas shells with radiation pressure
298 on dust in radiation-hydrodynamic simulations. *MNRAS* **473**, 4197–4219 (2018). 1703.05766.
- 299 [29] Ferrarese, L. & Merritt, D. A Fundamental Relation between Supermassive Black Holes and
300 Their Host Galaxies. *ApJL* **539**, L9–L12 (2000). astro-ph/0006053.
- 301 [30] Genzel, R. *et al.* Phibss: Molecular Gas, Extinction, Star Formation, and Kinematics in the $z =$
302 1.5 Star-forming Galaxy EGS13011166. *ApJ* **773**, 68 (2013). 1304.0668.
- 303 [31] Chartas, G. X-Ray Observations of Gravitationally Lensed Quasars: Evidence for a Hidden
304 Quasar Population. *ApJ* **531**, 81–94 (2000). astro-ph/9910299.
- 305 [32] Glikman, E. Red Quasars are in a Radiatively Driven Blow-out Phase. *Research Notes of the*
306 *American Astronomical Society* **1**, 48 (2017).
- 307 [33] Ricci, C. *et al.* The close environments of accreting massive black holes are shaped by radiative
308 feedback. *Nature* **549**, 488–491 (2017). 1709.09651.
- 309 [34] McMullin, J. P., Waters, B., Schiebel, D., Young, W. & Golap, K. CASA Architecture and
310 Applications. In Shaw, R. A., Hill, F. & Bell, D. J. (eds.) *Astronomical Data Analysis Software*
311 *and Systems XVI*, vol. 376 of *Astronomical Society of the Pacific Conference Series*, 127 (2007).

- 312 [35] Barvainis, R., Alloin, D., Guilloteau, S. & Antonucci, R. Detection of CO (3–2) Emission at $z =$
313 2.64 from the Gravitationally Lensed Quasar MG 0414+0534. *ApJL* **492**, L13–L16 (1998).
314 [astro-ph/9710326](https://arxiv.org/abs/astro-ph/9710326).
- 315 [36] Calistro Rivera, G., Lusso, E., Hennawi, J. F. & Hogg, D. W. AGNfitter: A Bayesian MCMC
316 Approach to Fitting Spectral Energy Distributions of AGNs. *ApJ* **833**, 98 (2016). [1606.05648](https://arxiv.org/abs/1606.05648).
- 317 [37] Prevot, M. L., Lequeux, J., Maurice, E., Prevot, L. & Rocca-Volmerange, B. The typical
318 interstellar extinction in the Small Magellanic Cloud. *A&A* **132**, 389–392 (1984).
- 319 [38] Kochanek, C. S. *et al.* The CASTLES Survey (1999). URL
320 <https://www.cfa.harvard.edu/castles/>.
- 321 [39] Stacey, H. R. *et al.* Gravitational lensing reveals extreme dust-obscured star formation in quasar
322 host galaxies. *MNRAS* **476**, 5075–5114 (2018). [1705.10530](https://arxiv.org/abs/1705.10530).
- 323 [40] Dale, D. A., Helou, G., Contursi, A., Silbermann, N. A. & Kolhatkar, S. The Infrared Spectral
324 Energy Distribution of Normal Star-forming Galaxies. *ApJ* **549**, 215–227 (2001).
- 325 [41] Kennicutt, R. C., Jr. The Global Schmidt Law in Star-forming Galaxies. *ApJ* **498**, 541–552
326 (1998). [astro-ph/9712213](https://arxiv.org/abs/astro-ph/9712213).
- 327 [42] Riechers, D. A., Walter, F., Carilli, C. L. & Lewis, G. F. Imaging The Molecular Gas in a $z =$
328 3.9 Quasar Host Galaxy at $0''.3$ Resolution: A Central, Sub-Kiloparsec Scale Star Formation
329 Reservoir in APM 08279+5255. *ApJ* **690**, 463–485 (2009). [0809.0754](https://arxiv.org/abs/0809.0754).
- 330 [43] Narayanan, D. & Krumholz, M. R. A theory for the excitation of CO in star-forming galaxies.
331 *MNRAS* **442**, 1411–1428 (2014). [1401.2998](https://arxiv.org/abs/1401.2998).
- 332 [44] Hung, C.-L. *et al.* What drives the evolution of gas kinematics in star-forming galaxies?
333 *MNRAS* **482**, 5125–5137 (2019). [1806.04233](https://arxiv.org/abs/1806.04233).
- 334 [45] Neeleman, M. *et al.* The Kinematics of $z \gtrsim 6$ Quasar Host Galaxies. *ApJ* **911**, 141 (2021).
335 [2102.05679](https://arxiv.org/abs/2102.05679).

- 336 [46] Madden, S. C. *et al.* Tracing the total molecular gas in galaxies: [CII] and the CO-dark gas.
337 *A&A* **643**, A141 (2020). 2009.00649.
- 338 [47] Rizzo, F., Vegetti, S., Fraternali, F., Stacey, H. R. & Powell, D. Dynamical properties of $z \sim 4.5$
339 dusty star-forming galaxies and their connection with local early-type galaxies. *MNRAS* **507**,
340 3952–3984 (2021). 2102.05671.
- 341 [48] Fraternali, F. *et al.* Fast rotating and low-turbulence discs at $z = 4.5$: Dynamical evidence of
342 their evolution into local early-type galaxies. *A&A* **647**, A194 (2021). 2011.05340.
- 343 [49] Kim, D., Im, M., Glikman, E., Woo, J.-H. & Urrutia, T. Accretion Rates of Red Quasars from
344 the Hydrogen $P\beta$ Line. *ApJ* **812**, 66 (2015). 1510.03887.
- 345 [50] Fabian, A. C. The obscured growth of massive black holes. *MNRAS* **308**, L39–L43 (1999).
346 astro-ph/9908064.
- 347 [51] Bieri, R. *et al.* Outflows driven by quasars in high-redshift galaxies with radiation
348 hydrodynamics. *MNRAS* **464**, 1854–1873 (2017). 1606.06281.
- 349 [52] Costa, T., Pakmor, R. & Springel, V. Powering galactic superwinds with small-scale AGN
350 winds. *MNRAS* **497**, 5229–5255 (2020). 2006.05997.
- 351 [53] Fabian, A. C., Vasudevan, R. V., Mushotzky, R. F., Winter, L. M. & Reynolds, C. S. Radiation
352 pressure and absorption in AGN: results from a complete unbiased sample from Swift. *MNRAS*
353 **394**, L89–L92 (2009). 0901.0250.
- 354 [54] Stacey, H. R., Lafontaine, A. & McKean, J. P. Smoke on the water: CO and H₂O in a
355 circumnuclear disc around a quasar at redshift 2.64. *MNRAS* **493**, 5290–5300 (2020).
356 2002.07186.
- 357 [55] King, A. R. Black hole outflows. *MNRAS* **402**, 1516–1522 (2010). 0911.1639.
- 358 [56] Faucher-Giguère, C.-A. & Quataert, E. The physics of galactic winds driven by active galactic
359 nuclei. *MNRAS* **425**, 605–622 (2012). 1204.2547.

- 360 [57] Chartas, G. *et al.* Multiphase Powerful Outflows Detected in High-z Quasars. *ApJ* **920**, 24
361 (2021). 2106.14907.
- 362 [58] Dadina, M. *et al.* Yet another UFO in the X-ray spectrum of a high-z lensed QSO. *A&A* **610**,
363 L13 (2018). 1801.09839.
- 364 [59] Sharon, C. E. *et al.* A Total Molecular Gas Mass Census in $z \sim 2-3$ Star-forming Galaxies:
365 Low-J CO Excitation Probes of Galaxies' Evolutionary States. *ApJ* **827**, 18 (2016).
366 1606.02309.
- 367 [60] Riechers, D. A. Molecular Gas in Lensed $z > 2$ Quasar Host Galaxies and the Star Formation
368 Law for Galaxies with Luminous Active Galactic Nuclei. *ApJ* **730**, 108 (2011). 1101.5624.
- 369 [61] Riechers, D. A. *et al.* CO($J = 1 \rightarrow 0$) in $z > 2$ Quasar Host Galaxies: No Evidence for Extended
370 Molecular Gas Reservoirs. *ApJL* **739**, L32 (2011). 1106.2553.
- 371 [62] Virtanen, P. *et al.* SciPy 1.0: Fundamental Algorithms for Scientific Computing in Python.
372 *Nature Methods* **17**, 261–272 (2020).
- 373 [63] Harris, C. R. *et al.* Array programming with NumPy. *Nature* **585**, 357–362 (2020).
- 374 [64] Hunter, J. D. Matplotlib: A 2d graphics environment. *Computing in Science & Engineering* **9**,
375 90–95 (2007).
- 376 [65] Wenger, M. *et al.* The SIMBAD astronomical database. The CDS reference database for
377 astronomical objects. *A&AS* **143**, 9–22 (2000). astro-ph/0002110.
- 378 [66] Ochsenbein, F. *et al.* The VizieR database of astronomical catalogues.
- 379 [67] Hezaveh, Y. D. *et al.* ALMA Observations of SPT-discovered, Strongly Lensed, Dusty,
380 Star-forming Galaxies. *ApJ* **767**, 132 (2013). 1303.2722.
- 381 [68] Spilker, J. S. *et al.* ALMA Imaging and Gravitational Lens Models of South Pole
382 TelescopeSelected Dusty, Star-Forming Galaxies at High Redshifts. *ApJ* **826**, 112 (2016).
383 1604.05723.

- 384 [69] Shajib, A. J. *et al.* STRIDES: a 3.9 per cent measurement of the Hubble constant from the
385 strong lens system DES J0408-5354. *MNRAS* **494**, 6072–6102 (2020). 1910.06306.
- 386 [70] Blackburne, J. A., Pooley, D., Rappaport, S. & Schechter, P. L. Sizes and Temperature Profiles
387 of Quasar Accretion Disks from Chromatic Microlensing. *ApJ* **729**, 34 (2011). 1007.1665.
- 388 [71] Stacey, H. R. & McKean, J. P. A flux-ratio anomaly in the CO spectral line emission from
389 gravitationally lensed quasar MG J0414+0534. *MNRAS* **481**, L40–L44 (2018). 1808.05571.
- 390 [72] Tuan-Anh, P. *et al.* On the dust and gas components of the $z = 2.8$ gravitationally lensed quasar
391 host RX J0911.4+0551. *MNRAS* **467**, 3513–3524 (2017). 1609.03271.
- 392 [73] Sluse, D., Hutsemékers, D., Courbin, F., Meylan, G. & Wambsganss, J. Microlensing of the
393 broad line region in 17 lensed quasars. *A&A* **544**, A62 (2012). 1206.0731.
- 394 [74] Glikman, E. *et al.* A highly magnified gravitationally lensed red quasar at $z = 2.5$ with
395 significant flux anomaly: Uncovering a missing population. *arXiv e-prints* arXiv:1807.05434
396 (2018). 1807.05434.
- 397 [75] Cornachione, M. A. *et al.* A Microlensing Accretion Disk Size Measurement in the Lensed
398 Quasar WFI 2026-4536. *ApJ* **895**, 125 (2020). 1911.06218.
- 399 [76] Bate, N. F. *et al.* HST imaging of four gravitationally lensed quasars. *MNRAS* **479**, 4796–4814
400 (2018). 1807.03553.
- 401 [77] Morgan, N. D. *et al.* WFI J2026-4536 and WFI J2033-4723: Two New Quadruple Gravitational
402 Lenses. *AJ* **127**, 2617–2630 (2004). astro-ph/0312478.
- 403 [78] Wu, X.-B. *et al.* An ultraluminous quasar with a twelve-billion-solar-mass black hole at redshift
404 6.30. *Nature* **518**, 512–515 (2015). 1502.07418.
- 405 [79] Wang, F. *et al.* Spatially Resolved Interstellar Medium and Highly Excited Dense Molecular
406 Gas in the Most Luminous Quasar at $z = 6.327$. *ApJ* **880**, 2 (2019). 1906.06801.
- 407 [80] Carniani, S. *et al.* Constraints on high-J CO emission lines in $z \sim 6$ quasars. *MNRAS* **489**,
408 3939–3952 (2019). 1902.01413.

- 409 [81] Leipski, C. *et al.* Complete Infrared Spectral Energy Distributions of Millimeter Detected
410 Quasars at $z > 5$. *ApJ* **772**, 103 (2013). 1305.3999.
- 411 [82] Gallerani, S. *et al.* X-ray spectroscopy of the $z = 6.4$ quasar SDSS J1148+5251. *MNRAS* **467**,
412 3590–3597 (2017). 1702.07349.
- 413 [83] Walter, F. *et al.* A kiloparsec-scale hyper-starburst in a quasar host less than 1 gigayear after the
414 Big Bang. *Nature* **457**, 699–701 (2009). 0902.0662.
- 415 [84] Banerji, M. *et al.* The discovery of gas-rich, dusty starbursts in luminous reddened quasars at z
416 ~ 2.5 with ALMA. *MNRAS* **465**, 4390–4405 (2017). 1610.04907.
- 417 [85] Banerji, M. *et al.* The interstellar medium properties of heavily reddened quasars and
418 companions at $z \sim 2.5$ with ALMA and JVL. *MNRAS* **479**, 1154–1169 (2018). 1805.09825.
- 419 [86] Li, J. *et al.* Probing the Full CO Spectral Line Energy Distribution (SLED) in the Nuclear
420 Region of a Quasar-starburst System at $z = 6.003$. *ApJ* **889**, 162 (2020). 1912.12813.
- 421 [87] Feruglio, C. *et al.* The dense molecular gas in the $z \sim 6$ QSO SDSS J231038.88+185519.7
422 resolved by ALMA. *A&A* **619**, A39 (2018). 1804.05566.